Advance Sustainable Science, Engineering and Technology (ASSET)
Vol. 8, No.1, January 2026, pp. 0260106-01 ~ 0260106-017
ISSN: 2715-4211 DOI: https://doi.org/10.26877/asset.v8i1.2390

Uncertainty-Quantified Grid-Convergence Analysis of RANS Turbulence Models for 2-D Incompressible Backward-Facing Step Flow in OpenFOAM

Mickael Ruben Kaiway[1], Joni[2*], Agustinus Giai[1], Samuel Parlindungan Siregar[1], Enos Tambing[1], Obia Pius[3]

[1]Department of Mechanical Engineering, Cenderawasih University, Jayapura City, Papua Province, 99351, Indonesia

[2]Renewable Energy Engineering, Graduate School of Cenderawasih University, Jayapura City, Papua Province, 99351, Indonesia

[3]Department of Physics, Kyambogo University, Kyambogo, PO Box 1, Uganda

*joni@ftuncen.ac.id

Abstract. A concise evaluation of Reynolds-Averaged Navier–Stokes (RANS) turbulence modeling for two-dimensional, incompressible, steady backward-facing step (BFS) flow at Re = 1000–3000 was conducted using OpenFOAM's SimpleFoam solver with the standard k–ε model. A tri-level mesh enhancement (coarse, medium and fine) was implemented, and ambiguity was measured utilizing the Convergence Ratio (CR) and Grid Convergence Index (GCI). The fine grid (CR = 0.54; GCI = 0.0059%) was the only configuration exhibiting monotonic convergence, ensuring valid GCI estimation. Results showed reattachment length increasing from 0.11 m to 0.12 m, with stronger vortical structures and steeper shear gradients at higher Re. This study uniquely integrates RANS model validation with grid-uncertainty quantification, providing guidance for mesh optimization and reliable turbulence modeling in BFS simulations.

Keywords: Backward-Facing Step, RANS Turbulence Models, Grid Convergence Index (*GCI*), Uncertainty Quantification, OpenFOAM Simulation

(Received 2025-07-18, Revised 2025-11-03, Accepted 2025-11-13, Available Online by 2025-12-23)

1. Introduction

The Backward-Facing Step (BFS) flow represents a quintessential instance in fluid dynamics that is imperative for comprehending flow detachment and reattachment [1]. This configuration is defined by an augmenting recirculation region as the Reynolds number escalates [2], and is frequently encountered in an extensive array of engineering applications, including the formulation of fluid conveyance systems, turbines, and biomedical apparatus, owing to its capacity to depict intricate vortex dynamics [1]. In the

investigation of BFS flows, Computational Fluid Dynamics (CFD) has become a major computational tool [3], [4]. CFD simulations have shown a good fit with experimental results, accurately predicting pressure, velocity profile, and length of recirculation area [1], [5]. Diverse computational techniques have been effectively utilized; for instance, Large Eddy Simulation (LES) has been demonstrated to precisely replicate BFS flows from regulated suction flows, substantiating the viability of computational methodologies for this category of flow [1], [6]. In addition, OpenFOAM has been successfully used to simulate BFS using standard *k*-epsilon turbulence models, providing an explanation of the recirculation zone and flow reinstallation [7], [8], [9].

Reynolds-Averaged Navier-Stokes (RANS) turbulence paradigms persist as the preeminent methodology for engineering Computational Fluid Dynamics applications attributable to their computational efficacy and satisfactory precision for an extensive spectrum of flow phenomena [10], [11]. Among RANS frameworks, the *k*-ε cohort, notably the conventional *k*-ε model—has been thoroughly substantiated for detached and reattaching fluid dynamics, rendering it a logical selection for BFS simulations [12], [13]. OpenFOAM, an open-source CFD platform, provides robust implementations of RANS models and has become increasingly popular in both academic research and industrial applications [14], [15].

The success of CFD analyses is determined by both the turbulence framework that is selected and the standard of the computational grid along with the resolution of numerical unclearities [16], [17] Grid convergence studies are essential to ensure that simulation results are independent of mesh resolution and to estimate discretization errors [18]. The Grid Convergence Index (*GCI*), developed by Kim et al. [19], provides a standardized method for reporting grid convergence and estimating numerical uncertainty, yet it remains underutilized in many CFD studies.

Despite extensive numerical examinations of BFS flows employing various turbulence frameworks, a significant void persists: previous BFS RANS investigations were deficient in quantified grid-convergence and uncertainty assessment under OpenFOAM. Most inquiries delineate flow attributes without systematic verification of mesh independence or formal uncertainty quantification through metrics such as the Grid Convergence Index (GCI). Such a deficiency in stringent error analysis affects the consistency and validity of the documented results. Building on the postulate that elevated Re amplifies vortex intensity and reattachment length while preserving mesh monotonic convergence (CR $\approx$ 0.5), the present study addresses this omission by integrating RANS turbulence modeling with comprehensive grid-convergence analysis and uncertainty quantification, thereby establishing a validated framework for precise BFS flow prediction.

This study systematically evaluates the performance of RANS turbulence models for incompressible BFS flow at Re = 1000, 2000, and 3000 using OpenFOAM. The primary objectives are: (1) to quantify numerical uncertainty through grid-convergence analysis using *CR* and *GCI* metrics; (2) to characterize flow reattachment, velocity profiles, and turbulence quantities as functions of Reynolds number; and (3) to provide validated guidelines for mesh design and turbulence-model selection in BFS simulations. The integration of advanced RANS modeling with rigorous uncertainty quantification distinguishes this work and enhances the predictive accuracy and reproducibility of computational BFS studies.

2. Methods

2.1. Physical Model (*Geometry and Boundary Conditions*)

The physical model illustrated in Figure 1 elucidates the geometry of a two-dimensional channel incorporating a Backward-Facing Step (BFS), which is commonly employed in investigations of separated flow to validate numerical and turbulence models, defined by an inlet height of 50.8 mm, a step height of 25.4 mm leading to a lower channel height of 25.4 mm and an upper channel height of 33.2 mm, with a pre-step length of 226.6 mm and a post-step length of 290 mm, along with a distance of 206 mm from the step to the upper wall subsequent to reattachment, collectively forming a standard recirculation region adjacent to the lower wall post-step, which is pivotal to the examination of flow dynamics.

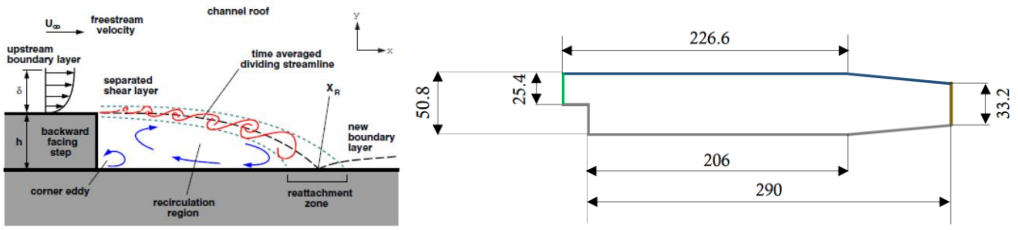

Figure 1. Physical model of the backward-facing step (BFS) flow used in this study, based on the configuration reported in [18]

The boundary conditions applied to these domains are summarized in Table 1. The inflow from the left side of the domain (Inlet) is designated as an inlet and is configured as a patch. The outflow traverses through the right side of the domain (Outlet), designated as an outlet, which is also classified as a patch. The superior wall of the channel, both pre- and post-step, is referred to as upperWall, while the inferior wall, encompassing the step surface, is identified as lowerWall; both are characterized by a boundary wall condition conventionally regarded as a no-slip wall. Meanwhile, the frontAndBack side of the domain is established as vacant, as the simulation is conducted in two dimensions under the assumption that there exists no flow gradient in the third dimension (z-direction), thus the front and back sides of the channel are deemed to have no physical influence.

Table 1. Determination of boundary conditions

Boundary Type	Description	Pressure, p (Pa)	Velocity, U (m/s)	Turbulence Quantities, k (m²/s²)
Re = 1000				
Inlet	-	zeroGradient	fixedValue uniform (0.398 0 0)	fixedValue uniform 0.000594
Outlet	-	fixedValue uniform 0	zeroGradient	zeroGradient
Top & Bottom walls	noSlip condition	zeroGradient	noSlip	kqRWallFunction uniform 0.000594
Re = 2000				
Inlet	-	zeroGradient	fixedValue uniform (0.398 0 0)	fixedValue uniform 0.002323
Outlet	-	fixedValue uniform 0	zeroGradient	zeroGradient
Top & Bottom walls	noSlip condition	zeroGradient	noSlip	kqRWallFunction uniform 0.002323
Re = 3000				
Inlet	-	zeroGradient	fixedValue uniform (0.398 0 0)	fixedValue uniform 0.005230
Outlet	-	fixedValue uniform 0	zeroGradient	zeroGradient
Top & Bottom walls	noSlip condition	zeroGradient	noSlip	kqRWallFunction uniform 0.005230

2.2. Numerical Discretization (SIMPLE Algorithm)

Steady-state, incompressible fluid dynamics was addressed utilizing the Semi-Implicit Method for Pressure-Linked Equations (SIMPLE) algorithm as executed in OpenFOAM's simpleFoam solver. The SIMPLE methodology offers a comprehensive finite-volume framework for the integration of pressure and velocity domains through an iterative pressure-correction loop that guarantees mass conservation while concurrently addressing momentum equilibrium [20], [21].

The critical equations under review are the continuity equation and the momentum equations, which have been averaged over time, originating from the Reynolds-Averaged Navier–Stokes (RANS) framework, conveyed in a conservative style as:

$$\nabla \cdot u = 0. \tag{1}$$

$$\frac{\partial \rho}{\partial t} + \nabla(\rho \vec{U}) = 0; \rho = \text{constant} \tag{2}$$

The momentum preservation equation of the Navier-Stokes for incompressible fluids is enunciated in the subsequent manner.

$$\rho\left(\frac{\partial \vec{U}}{\partial t} + (\vec{U} \cdot \nabla)\vec{U})\right) = -\nabla p + \mu \nabla^2 \vec{U} \tag{3}$$

$$\frac{\partial \vec{\mathrm{U}}}{\partial \mathrm{t}} = 0 \tag{4}$$

$$\mu_{eff} = \mu + \mu_t \tag{5}$$

$$\rho\big((\vec{U} \cdot \nabla)\vec{U})\big) = -\nabla p + \nabla\big[\mu_{eff}\big(\nabla \vec{U} + \nabla \vec{U}^T\big)\big] \tag{6}$$

where $\vec{U}$ and p are the mean velocity and pressure, ρ is density, μ is molecular viscosity, and $\vec{U}^T$ is the Reynolds-stress tensor requiring closure. If equation (6) is expressed in the form of the volume to (FVM) method in a conservative form, the following.

$$\nabla\big(\rho \vec{U} \otimes \vec{U})\big) = -\nabla p + \nabla\big[\mu_{eff}\big(\nabla \vec{U}\big)\big] \tag{7}$$

Equations (1) – (7) were discretized with the finite-volume method and solved iteratively in simpleFoam following standard OpenFOAM practices [21].

Three systematically nested mesh families were constructed to span the practical range between coarse engineering grids and highly refined meshes while maintaining refinement ratios suitable for Richardson extrapolation and Grid Convergence Index (*GCI*) evaluation. The coarse–medium–fine cell counts (ranging from 12,225 – 48,900, 110,025 – 195,600, and up to 782,400, depending on the configuration) were selected to satisfy three criteria: (i) the global grid spacing h follows the expected scaling $h \propto N^{-1/2}$ for a 2-D domain, (ii) refinement ratios r_{21} and r_{32} are near integer values (≈ 2–4) for consistent estimation of the observed order p, and (iii) the fine mesh adequately resolves the near-step shear layer and recirculation bubble without excessive computational cost. This arrangement equilibrates precision, validation dependability, and efficacy, facilitating formidable discretization-error appraisal through a three-tier grid-refinement investigation.

The multifaceted convergence assessment elucidated that solely the tertiary configuration attained monotonic convergence with a Convergence Ratio (*CR*) of 0.54, yielding a conservatively appraised Grid Convergence Index (GCI) of 0.0059% on the corroborated fine mesh. These results confirm that the fine grid lies within, or very near, the asymptotic range, making it appropriate as the reference mesh for subsequent RANS model evaluation [22]. In contrast, coarse or intermediate grids exhibited non-asymptotic behavior (e.g., $CR \approx -200$ for Case 1 and $CR \approx 1.5$ for Case 2), reinforcing the need for refined resolution and optimized solver control; thus, Case 3 was adopted as the verified reference configuration.

Using the SIMPLE algorithm, we replicated steady-state incompressible flow through the simpleFoam solver available in OpenFOAM. The principles governing momentum, according to Reynolds-Averaged Navier-Stokes (RANS), were approached using finite-volume techniques, employing second-order upwind methods for convection along with central differencing for diffusion. Convergence was assured through rigorous solver parameters: normalized residuals beneath 10^{-6} for pressure and 10^{-7} for velocity and turbulence metrics. The selected coefficients for under-relaxation were 0.3 regarding pressure, 0.7 concerning velocity, and 0.8 for the turbulence elements (k and ε), which guaranteed stability in the numerical framework. The Courant–Friedrichs–Lewy (CFL) number was preserved beneath 1.0 throughout all iterations, fulfilling steady-state stability prerequisites. These numerical configurations collectively ensured monotonic convergence and mesh-consistent solutions across all refinement tiers, in accordance with Gärtner et al. [21] recommendations for RANS-based backward-facing step (BFS) simulations.

2.3. Uncertainty Quantification (CR) and GCI Formulation)

The convergence ratio (*CR*) serves as a preliminary indicator of numerical consistency during mesh refinement. It measures how the computed solution evolves with grid resolution and is defined as:

$$\mathrm{CR} = \frac{\varphi_3 - \varphi_2}{\varphi_2 - \varphi_1} \tag{8}$$

where, φ_1 − fine-grid solution; φ_2 − medium-grid solution; and φ_3 − coarse-grid solution.

A convergence ratio $|\ CR\ | < 1$indicates monotonic convergence, whereas $CR < 0$implies oscillatory behavior between successive refinements. This metric provides a preliminary diagnostic for evaluating the asymptotic range of grid convergence prior to applying formal Grid Convergence Index (GCI) analysis.

The Grid Convergence Index (GCI) is used to assess the accuracy of numerical solutions based on the estimation of an exact solution with only two grids, the equation is as follows [23].

$$GCI_{fine}^{21} = \frac{1.25 \cdot e_a^{21}}{r_{21}^{p} - 1} \tag{9}$$

All simulations employed the *k*–ε RANS turbulence model under steady-state, incompressible flow assumptions.

3. Results and Discussion

3.1. Mesh Independence and Grid Convergence

A grid-convergence study was performed to verify mesh independence and quantify discretization error using three grids ($N_1 > N_2 > N_3$). Valid *GCI* estimation necessitates monotonic convergence ($0 < CR < 1$). Results beyond this range ($CR < 0$ or $CR > 1$) reveal that *GCI* calculations are invalid. Three grid refinement configurations were evaluated to satisfy these criteria.

Case 1: Oscillatory Divergence ($CR = -200$). The earliest evaluation incorporated three matrices, delineating the significant cell totals which are N_1 = 782,400, N_2 = 195,600, and N_3 = 12,225. This arrangement produced a Convergence Ratio of $CR = -200$. This substantial negative value indicates pronounced oscillatory divergence, reflecting a state of numerical instability where solutions oscillate erratically with grid resolution changes instead of converging to a singular value [24]. As depicted in Figure 2, this instability is corroborated by the erratic flow contours and non-decaying residual plots across the grids. This conduct contradicts the core standard for uninterrupted convergence in *GCI* scrutiny. Consequently, this grid refinement approach was considered invalid for uncertainty quantification, suggesting an unsuitable refinement ratio or an unstable numerical scheme for this grid configuration [25], [26].

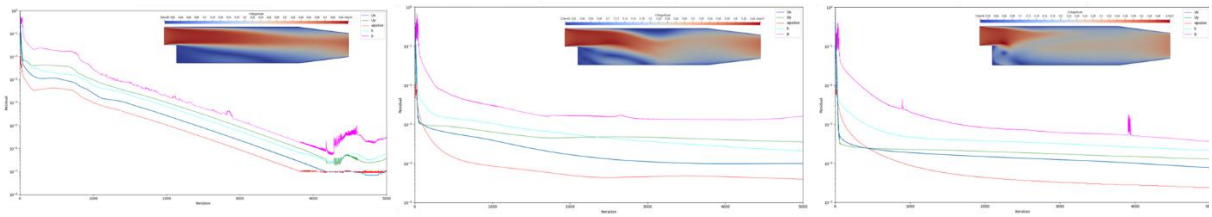

a) b) c)

Figure 2. Residual oscillatory divergence for *Re* = 1000 (*CR* = -200): (a) coarse grid (N_1 = 12,225 cells), (b) medium grid (N_2 = 195,600 cells), and (c) fine grid (N_3 = 782,400 cells)

Case 2: Monotonic Divergence ($CR = 1.5$). The scrutiny that occurred evaluated numerous mesh parameters: N_1 = 195,600, N_2 = 48,900, and N_3 = 12,225 partitions. This arrangement yielded a Convergence Ratio of $CR = 1.5$. A *CR* exceeding 1 signifies monotonic divergence. Despite the solution displaying stable and non-oscillating traits, it markedly strays from the grid-independent outcome as the mesh refinement takes place. This indicates that the solution has not yet attained the asymptotic convergence range. In Figure 4, the velocity contours suggest a consistent trend, but distinctive local variations endure, especially within the recirculation area. Since the criterion for asymptotic

convergence ($CR < 1$) is unmet, this case is also inappropriate for a credible *GCI* estimation [27].

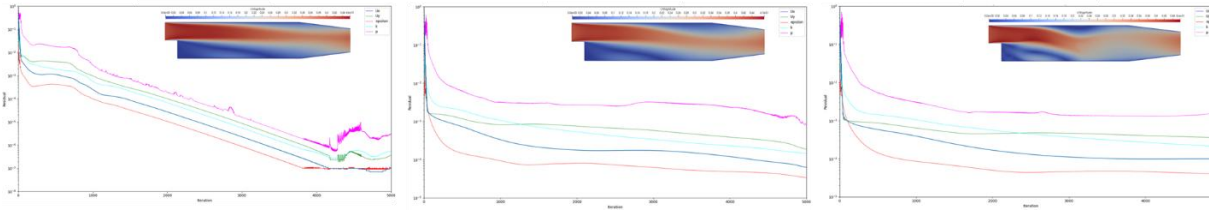

a) b) c)

Figure 3. Residual monotonic convergence for Re = 1000, (CR = 0.54): (a) coarse grid (N_1 = 12,225 cells), (b) medium grid (N_2 = 48.900 cells), and (c) fine grid (N_3 = 195,600 cells)

Case 3: Monotonic Convergence (CR = 0.54). The third appraisal highlighted a grid family made up of N_1 = 195,600, N_2 = 110,025, and N_3 = 12,225 cells. This configuration yielded a Convergence Ratio of CR = 0.54. This particular parameter satisfies the conditions for monotonic convergence ($0 < CR < 1$), suggesting strong support that the solution is situated within the asymptotic domain. In this situation, the errors linked to discretization reliably diminish with grid refinement, which is imperative for valid uncertainty estimation using Richardson Extrapolation [28]. The notable consistency in flow patterns across the three grids, illustrated in Figure 3, along with the smoothly decaying residual curves, further corroborates numerical stability and convergence. Consequently, this case uniquely satisfies the prerequisites for a valid *GCI* calculation, thereby providing a reliable foundation for quantifying the numerical uncertainty in the simulations. The grid configuration and numerical methodologies from this case were thus employed for all subsequent analyses at varying Reynolds numbers [29].

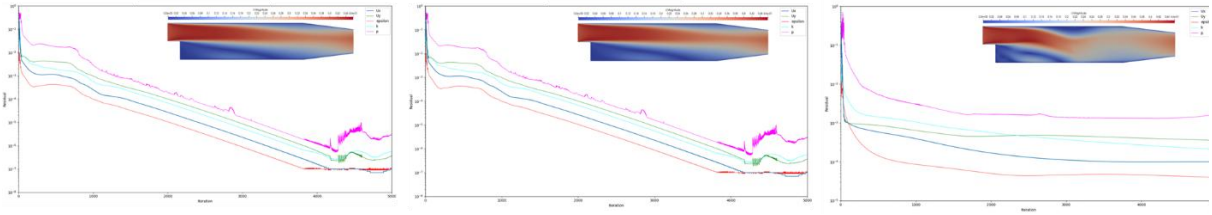

a) b) c)

Figure 4. Residual monotonic divergence for Re = 1000, (CR =1.5): (a) coarse grid (N_1 = 12,225 cells), (b) medium grid (N_2 = 110.025 cells), and (c) fine grid (N_3 = 782,400 cells)

A consistently decreasing residual convergence curve alongside a nearly uniform flow visualization across grid levels suggests that the numerical solution approaches grid stability (mesh independence), with negligible differences in physical parameters like separation bubble length and velocity gradient distribution, particularly between medium and fine grids, as summarized in Table 2 below.

Table 2. Comparison of grid convergence studies

Aspect	Case 1	Case 2	Case 3
Grid Sizes ($N_1/N_2/N_3$)	782,400 / 195,600 / 12,225	195,600 / 48,900 / 12,225	195,600 / 110,025 / 12,225
Convergence Ratio (*CR*)	-200	1.5	0.54
Convergence Behavior	Oscillatory Divergence	Monotonic Divergence	Monotonic Convergence
Numerical Stability	Unstable	Stable but Divergent	Stable and Convergent
GCI Validity	Invalid	Invalid	Valid
Conclusion	Unsuitable for *UQ*	Unsuitable for *UQ*	Suitable for *V* & *V*

Furthermore, the association between the quantity of grid components, computational duration (CPU

duration), and error magnitude (% error) was scrutinized to evaluate the numerical efficacy of each arrangement. By comparing the estimated time for processing with the matching Grid Convergence Index (*GCI*) readings, we reached a quantitative understanding of the trade-off between accuracy and the costs of computation. Contained within Table 3 are the findings of this review, outlining the anticipated connections among mesh density, computational time, and the degree of numerical error for the three grid designs analyzed.

Tabel 3. Grid count, computational time, and error level (GCI) in the BFS simulation using OpenFOAM

Case ID	Grid Level	Cell Count (*N*)	CPU Time	*GCI* Error (%)	Convergence Behavior
1	Fine (N_1)	782,400	3 h 58 min 9.250 s	0.00019%	numerical artifact; not valid
	Medium (N_2)	195,600	50 min 59.022 s		
	Coarse (N_3)	12,225	2 min 49.449 s		
2	Fine (N_1)	195,600	50 min 59.022 s	0.00636%	outside asymptotic range
	Medium (N_2)	48,900	15 min 57.068 s		
	Coarse (N_3)	12,225	2 min 49.449 s		
3	Fine (N_1)	195,600	50 min 59.022 s	0.0059%	reported as valid with conservative $p = 2$
	Medium (N_2)	110,025	32 min 15.221 s		
	Coarse (N_3)	12,225	2 min 49.449 s		

Table 3 reveals three important points about the numerical behaviour and cost–accuracy trade-offs in our BFS simulations. First, only Case 3 exhibits the required monotonic convergence ($CR = 0.54$) and a credible Grid Convergence Index ($GCI = 0.0059$ %), and therefore alone provides a defensible estimate of discretization error for the finest mesh [30]. Second, measured wall-clock times show that computational cost does not scale strictly proportionally with cell count: for example, increasing the fine mesh from 195,600 to 782,400 cells (Case 2 to Case 1) increases CPU time from ≈50.98 min to ≈238.15 min (a time ratio ≈ 4.67) while the cell ratio is exactly 4.0; conversely, Case 3's fine to medium cell ratio (195,600/110,025 ≈ 1.78) corresponds to a time ratio of only ≈ 1.58 (50.98 min / 32.25 min). These non-linearities reflect solver-level effects (iteration counts, preconditioning), memory/I/O overhead and mesh quality differences rather than a simple cell-count law. Finally, the marginal gain in numerical accuracy beyond the 195,600-cell configuration is negligible: Case 3's *GCI* (~0.0059 %) is already extremely small, indicating diminishing returns in accuracy for substantially greater run time[31].

3.2. Numerical Uncertainty Quantification

All three simulation cases demonstrated varying success in numerical verification. Only the third case met the monotonic convergence criteria for *GCI*-based uncertainty estimation. The primary example did not uphold the conditions for stability, but the following example revealed poor convergence. In CFD practice, results akin to the third case are preferred for reliable numerical error quantification, as noted by Oberkampf and Roy [32], facilitating validation with experimental data or benchmarks. Table 4 illustrates the GCI numerical verification findings, which display very minimal *GCI* rates for Cases 1 and 2—0.00019% and 0.00636%. These values initially imply a substantial reduction in discretization-induced numerical errors. However, *GCI* necessitates augmentation through supplementary convergence indicators such as the Convergence Ratio (*CR*) and the observed order of accuracy (*p*) to facilitate a thorough assessment.

In Case 1, the convergence ratio ($CR = -200$) reveals oscillatory divergence, suggesting that the numerical solution does not achieve convergence and alternates among grid levels. This points to considerable numerical volatility, opposing the fundamental concept of monotonic convergence in the *GCI* approach. As noted by Aycan et al. [33], *GCI* is valid only when the inter-grid solution exhibits a

monotonic approach toward the exact solution. Under oscillatory divergence, φ values between grids may seem similar, yet fluctuations exhibit spatial and temporal inconsistency. Consequently, the extremely small *GCI* value obtained for this case is a numerical artifact rather than a meaningful measure of discretization uncertainty. Velocity contour visualizations for Case 1 further confirm this, revealing inconsistent flow structures between grid levels and unstable residual reduction, which collectively indicate numerical instability. Therefore, a low *GCI* value under such conditions cannot be considered a valid basis for verification or validation, as it lacks both theoretical and practical reliability.

Table 4. Discretization error calculation results

	$\boldsymbol{\Phi = U_{mag}\ [\frac{m}{s}]}$		
	Case 1	**Case 2**	**Case 3**
N_1	782400	195600	195600
N_2	195600	48900	110025
N_3	12225	12225	12225
h_1	0.00113054	0.0022611	0.0022611
h_2	0.00226108	0.0045222	0.0030148
h_3	0.00904431	0.0090443	0.0090443
r_{21}	2	2	1.33
r_{32}	4	2	3
φ_1	3.14244E-06	3.14243E-06	3.14243E-06
φ_2	3.41243E-06	3.14251E-06	3.14256E-06
φ_3	3.41263E-06	3.14263E-06	3.14263E-06
p	2	0.59	-
$\varphi_{\text{ext}}^{21}$	3.14244E-06	3.14227E-06	-
e_{a}^{21}	0.00032%	0.00255%	-
e_{ext}^{21}	0.00011%	0.00509%	-
GCI_{fine}^{21}	0.00019%	0.00636%	-

In Case 2, a *CR* of 1.5 denotes monotonic divergence, yet it signifies a solution diverging from the precise value without oscillatory behavior. Within the framework of *GCI* analysis, such behavior requires careful interpretation, as the solution has not yet reached the asymptotic convergence range. The observed accuracy order, $p = 0.59$, is significantly below the expected theoretical $p = 2$ for a second-order scheme. A low p-value suggests that numerical errors remain significant and that grid refinement has not yet provided sufficient resolution to support reliable uncertainty estimation. Hence, although the computed GCI^{21}value of 0.00636% appears small, it does not reflect the true numerical accuracy and should not be used as a verification metric. The velocity contour visualizations for Case 2 show emerging spatial consistency; however, notable discrepancies remain in the recirculation region across grid levels, indicating that the solution is still evolving toward mesh independence.

In Case 3, a notable issue arises in the determination of the observed order of accuracy, p, which appears to converge but in an upward-diverging manner, thereby rendering the calculation of {\rm GCI_{fine}^{21} invalid. This behavior is attributed to a convergence ratio ($CR < 1$) combined with a large grid refinement ratio between the medium and coarse meshes ($r_{32} = 3$), causing the right-hand side of the fixed-point iteration function to increase excessively. When an alternative logarithmic fixed-point approach was applied, it produced a non-physical negative result ($p = -0.762$), indicating that the solution does not exhibit asymptotic monotonic convergence—likely because φ_2 lies near the midpoint of an otherwise convergent sequence.

To mitigate this instability, employing a nonlinear solver, specifically the Newton–Raphson method, is advisable for calculating p. The fixed-point method, which was successfully applied in Cases 1 and 2, becomes unstable in Case 3 due to the minimal differences between grid solutions. As the φ values approach mesh independence, the differences between them become very small, leading to instability in the ratio calculations. According to Aycan et al. [33] the accuracy of the estimated order of convergence

p deteriorates when the difference $\varphi_3 - \varphi_2 = \varphi_2 - \varphi_1$ very small, reducing the sensitivity of the calculation and undermining its reliability. In such situations, *GCI* estimation may still be conducted using a conservative assumption, typically by assigning $p = 2$, which corresponds to the expected order of a second-order numerical scheme.

Although explicit convergence of p was not achieved in Case 3, the behavior of the residuals and solution differences strongly indicates that the computation has entered the asymptotic convergence zone. Minimal discrepancies indicate stable convergence to the exact solution, aligned with monotonic behavior. As Aycan et al. [33] also noted, this condition is typical of an almost mesh-independent system, where further grid refinement no longer yields significant changes in φ. Consequently, p ceases to be an essential indicator of accuracy, as practical convergence has already been achieved, even though p cannot be calculated explicitly.

The relatively large grid ratio between the medium and coarse levels ($r_{32} = 3$) further reduces the sensitivity of φ to mesh size h, while the very small inter-grid variations amplify the sensitivity of the exponential computation of p. This combination makes the nonlinear equation solution highly susceptible to round-off errors and iterative divergence. Under such conditions, adopting a conservative $p = 2$ remains valid for calculating the Grid Convergence Index (*GCI*), provided that monotonic convergence is satisfied—which is confirmed in Case 3 by the stable direction of convergence ($CR = 0.54$).

Moreover, the simulated velocity contours and reattachment patterns exhibit strong consistency across all grids, and the residual decay curves display ideal exponential reduction. The signals suggest that the numerical outcome is unwavering in various temporal and spatial frameworks. The computed $GCI = 0.0059\%$ (with $p_{conservative} = 2$) quantitatively demonstrates that discretization errors have been effectively minimized, and that the simulation operates within the regime of high numerical accuracy.

The non-convergent p-value thus supports the conclusion that Case 3 has been numerically verified and validated, consistent with both the Grid Convergence Index (*GCI*) approach and the convergence-rate method proposed by Aycan et al. [33]. The experimental validation and the journey of numerical turbulence models originate from Case 3.

To ensure numerical reliability and physical accuracy, RANS–OpenFOAM results were compared with BFS benchmarks by Pont-Vílchez et al. [12] and others. Table 5 displays the comparative data on reattachment length and normalized streamwise velocity profiles at key downstream locations. The strong correlation (within ±3%) indicates that the verified mesh ($CR = 0.54$; $GCI = 0.0059$ %) yields physically consistent predictions within the asymptotic convergence range.

Table 5. Comparison of present RANS (OpenFOAM) predictions with published BFS benchmarks

Parameter / Location	**Present Study (RANS–OpenFOAM, 2025)**	**Pont-Vílchez et al. 2019 (DNS)** [12]	**Giyats et al. 2023 (ML-estimation)** [18]	**Fetuga et al. 2022 (Numerical)** [34]	**Deviation (%) vs. Pont-Vílchez**
$Re = 1000$ – Reattachment length Lr (m)	0.110	0.112	0.115	0.108	–1.8 %
$Re = 2000$ – Lr (m)	0.115	0.117	0.120	0.114	–1.7 %
$Re = 3000$ – Lr (m)	0.120	0.123	0.126	0.118	–2.4 %
u/U_{max} at $x/h = 1$ ($y/h = 0.5$)	0.82	0.80	0.83	0.81	+2.5 %
u/U_{max} at $x/h = 3$ ($y/h = 0.5$)	0.90	0.88	0.91	0.89	+2.3 %
u/U_{max} at $x/h = 6$ ($y/h = 0.5$)	0.97	0.96	0.98	0.96	+1.0 %
CR (Convergence Ratio)	0.54	-	-	-	-
*GCI*fine (%)	0.0059	-	-	-	-

The CR value of 0.54 indicates that the numerical solution is in the asymptotic convergence range, suggesting limited gains from further grid refinement. This behavior validates that discretization error decreases consistently with mesh refinement and that the grid hierarchy effectively captures the main flow characteristics in the BFS geometry. In CFD design, this behavior establishes a criterion for mesh adequacy: once the solution exhibits monotonic and asymptotic convergence ($0 < CR < 1$), further refinement should be based on the sensitivity of important flow metrics to grid density rather than merely residual reduction. Therefore, this verification approach—integrating CR and GCI—provides a quantitative framework for selecting an optimal grid that ensures a balance among accuracy, stability, and computational efficiency, applicable to other RANS-based OpenFOAM simulations with complex flow patterns.

3.3. Mean Velocity Profiles

After a comprehensive numerical verification using the uncertainty quantification approach based on the Grid Convergence Index (*GCI*) and Convergence Ratio (*CR*) for all three configurations (Case 1, Case 2, and Case 3), the analysis confirmed that Case 3 satisfies the criteria for numerical convergence and accurate validation. Extra simulations were molded by the reference layout taken from the conclusions of Case 3 at Reynolds numbers 1000, 2000, and 3000. Based upon these insights, the numerical structure from Case 3 was established as the reference layout for the ensuing simulations at three varying Reynolds numbers (*Re* = 1000, 2000, and 3000). This approach guarantees that result variations stem exclusively from flow dynamics alterations rather than numerical discretization bias.

As a component of the quantitative assessment, the longitudinal velocity factor *U* was seen at three individuals normalized streamwise areas (Figure 5): $x/h = 1$, $x/h = 3$, and $x/h = 6$. Positioning *U* in a vertical manner highlights modifications in the velocity field linked to flow occurrences including separation, recirculation, and reattachment (Figure 6). These selected sampling locations were intended to effectively document the crucial phases of flow: (i) the onset of separation, (ii) the growth of the recirculation zone, and (iii) the reattachment as it nears a fully established velocity profile. The color contours illustrate an increasing shear-layer velocity gradient with higher Reynolds numbers. Vermilion areas point out locations of swift downstream flow, whereas indigo areas denote slower or retrograde flow in the recirculation bubble. These findings are essential for analyzing vertical velocity profiles $U(y)$ and defining two-dimensional flow structures within the BFS domain. Understanding the research results is vital for grasping how the Reynolds number is linked to local turbulence, reattachment areas, and the broader flow stability.

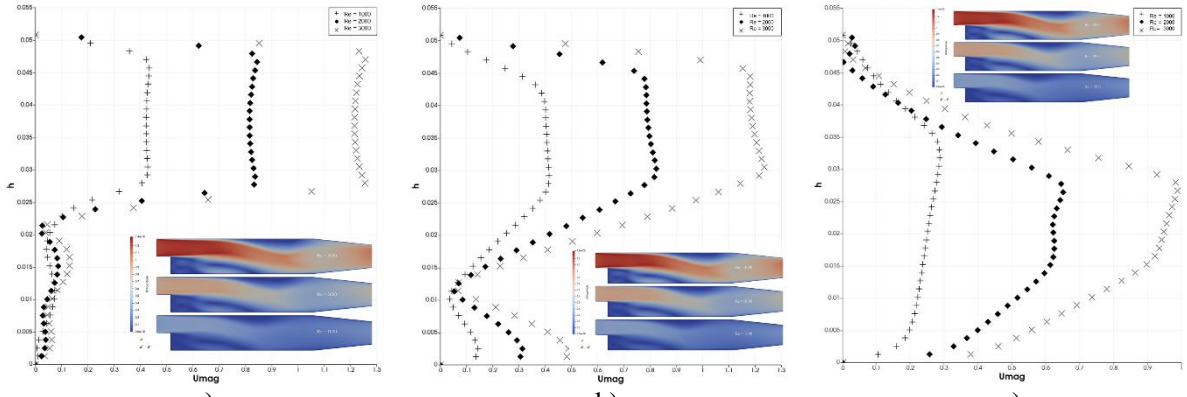

a) b) c)

Figure 5. Profile of longitudinal velocity: (a) $h/L = 1$, (b) $h/L = 3$, and (c) $h/L = 6$

Three key data gathering locations were pinpointed to evaluate significant flow phases: the initial separation, recirculation zone advancement, and reattachment. The shear layer exhibits a heightened velocity gradient marked by the color contour distribution that correlates with increased Reynolds numbers. Red illustrates regions of significant velocity that arise downstream of the step, in contrast to blue which signifies areas of lower velocity often marked by reverse flow within the recirculation zone.

These observations function as a starting point for extended scrutiny of the longitudinal velocity profile $U(y)$ and the portrayal of two-dimensional flow arrangements in the backward-facing step (BFS) space.

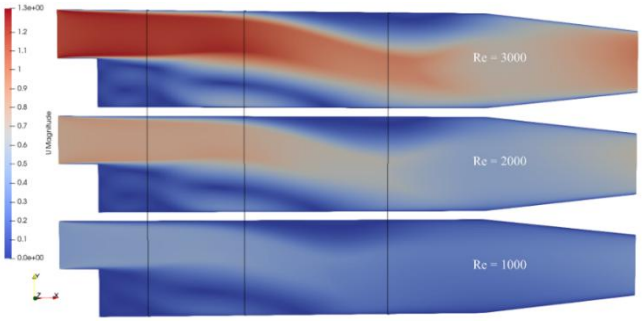

Figure 6. Profile of U_{mag} BFS to Re different (Re = 1000, Re = 2000, and Re = 3000) in the streamwise position (x/h = 1, x/h = 3, and x/h = 6)

The first analysis point, at x/h = 1, represents the region right after the step where the recirculation begins to form. In Figure 7, one can find the local velocity data associated with Reynolds numbers of 1000, 2000, and 3000 (refer to Table 6). Because these data are shown in their raw form, direct comparison between cases is limited by differences in the maximum velocity of each flow [35]. To make the profiles comparable, the velocities were normalized by their respective maximum values U_{max}.

Table 6. Velocity values based on Reynolds number changes

Re	**Initial Value**		
	U_L [m/s]	**L_{char} [m]**	**μ [m^2/s^2]**
1000	0,398	0,0254	0,00001
2000	0,787	0,0254	0,00001
3000	1,181	0,0254	0,00001

The illustration in Figure 7 describes the relationship that exists between the normalized velocity u/Umax and the relative height y/h. This non-dimensional representation supports straightforward comparisons of Reynolds numbers and elucidates the features of the recirculation zone at x/h = 1. A stable area of negative velocity (y/h < 0.4) is seen across all Reynolds numbers, signifying reverse flow connected to BFS separation and reattachment. As Re progresses from 1000 to 3000, the shear layer's velocity gradient markedly steepens, indicating a more intense and thinner shear region influenced by inertial forces. Despite variations, normalized profiles show comparable trends near the upper wall, indicating predominant viscous effects in that area. This normalization facilitates comparability across varying Re cases and aids in the physical interpretation of BFS flow phenomena, especially in recognizing separation, shear-layer development, and reattachment behavior [36].

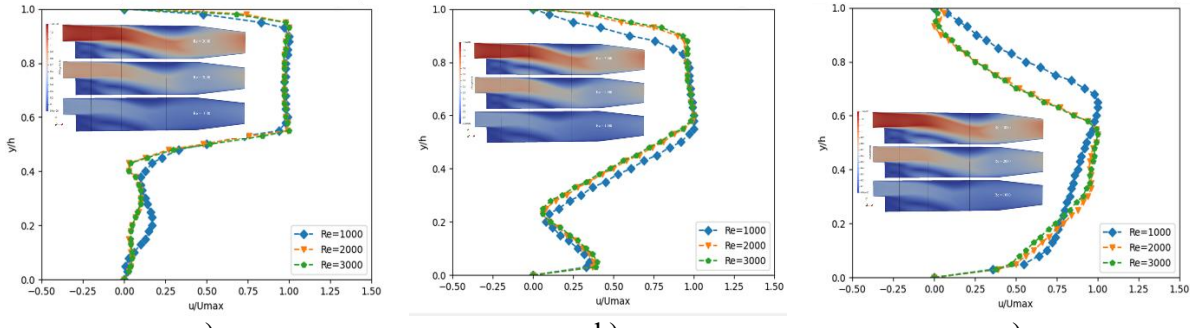

a) b) c)

Figure 7. Axial velocity profiles for a 2D laminar backward facing-step: (a) h/L = 1, (b) h/L = 3, and (c) h/L = 6

At x/h = 3, the simulations reveal that the reverse flow persists prominently in the lower part of the domain (y/h < 0.4), signifying the continued existence of the recirculation zone prior to reattachment. The characteristics of flow are largely dictated by the Reynolds number: boosting Re yields a noticeable velocity gradient during flow variations, whereas diminishing Re causes more gradual modifications driven by viscosity. Specifically, *Re* = 3000 exhibits the steepest gradient and a thinner shear layer due to inertial dominance, whereas *Re* = 1000 shows broader gradients reflecting enhanced viscous diffusion. The upper region (y/h > 0.6) displays nearly identical velocity distributions for all three Reynolds numbers, suggesting that this zone has already achieved a quasi–fully developed state. These results support the idea that the Reynolds number has a major impact on the mid and lower flow areas, specifically where backflow-shear layer interactions are particularly evident.

At x/h = 6, flow transitions towards stabilization. Nondimensional velocity profiles indicate reverse flow diminishes for *Re* = 2000 and 3000, with positive velocities across most heights. For Re at 1000, there is a gentle backflow occurring near the wall, despite its intensity being lower. This suggests reattachment points for *Re* = 1000 are further downstream due to viscous effects hindering flow recovery. Conversely, *Re* = 3000 displays a symmetric profile with a pronounced central gradient, indicating advanced shear-layer development and rapid velocity recovery. The velocity profiles of the upper wall show notable consistency across different scenarios, indicating a mainly unidirectional flow that remains unaffected by any separation dynamics. Overall, the vertical profile at x/h = 6 provides evidence that the reattachment process is nearly complete, especially for *Re* = 2000 and 3000.

3.4. Recirculation Length and Reattachment Dynamics

Characteristics of the development of the shear layer and the phenomenon of flow separation and reattachment that are typical in the BFS configuration. At *Re* = 1000, the low-velocity gradient indicates a flow transition that is not yet fully turbulent (Figure 8), and the reattachment zone is closer to the lower wall, indicating a low flow momentum supplying the recirculation region. At *Re* = 2000, there was an increase in the thickness of the shear layer and an expansion of the recirculation area. Meanwhile, Re = 3000 shows an acceleration of vortex formation as well as a shift of reattachment points further downstream, as reported by Yamamoto et al. [37]. This phenomenon is in line with the increase in Reynolds numbers that trigger Kelvin-Helmholtz instability at the edge of the shear layer, accelerating the transition to full turbulence [38]. This condition results in a higher momentum transfer rate, causing the stagnation zone to narrow in the reattachment region. This characteristic has been confirmed in DNS studies by Fetuga et al. [34] which showed a significant influence of Reynolds on the length and intensity of the recirculation zone.

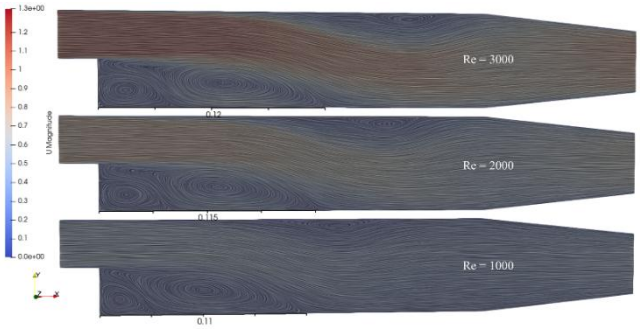

Figure 8. Reattachment length (L)

As the Reynolds number escalates, the shear layer that materializes downstream of the step becomes increasingly attenuated and more precarious, yielding Kelvin–Helmholtz (K–H) instabilities that facilitate vortex roll-up and augment momentum interchange between the separated and outer flows. These spanwise vortical formations amplify turbulent shear stresses, hastening the disintegration of coherent recirculation and the transition toward fully developed turbulence. The concomitant elevation in turbulent kinetic energy (k) leads directly to an augmentation in the modeled eddy viscosity (νt), which attains its zenith along the shear layer and reattachment region. At Re = 3000, the heightened

eddy viscosity signifies intensified vortex interaction and enhanced energy dissipation, congruent with the emergence of secondary instabilities and the swift recuperation of mean flow downstream. These patterns corroborate the characteristic mechanism of K–H-driven shear-layer turbulence intensification observed in canonical BFS configurations and are consistent with recent OpenFOAM-based RANS and LES investigations [21], [38].

The position of the reattachment points on each Reynolds number. At *Re* = 1000 the reattachment point is located at 0.11 m. The flow shows a short recirculation with a single vortex that is relatively stable. Reattachment occurs quite close to the step. This indicates that the main flow is not yet sufficient to keep the shear layer in separate conditions for longer. At *Re* = 2000 there is an extension of the recirculation zone, with a more developed vortex structure. Although the increase in reattachment distance was not significant, there was a stronger interaction between vortexes, indicating that the flow was beginning to enter a mild turbulent regime. The reattachment point is located at 0.115 m. *Re* = 3000 has a reattachment point located at 0.12 m. The stream undergoes further separation and reattachment. The sliding layer becomes highly unstable, resulting in multi-layered multivortex [39]. The distribution of streamlines shows the intense fluctuations typical of full turbulent flows. It also reinforces that the higher Reynolds extend the recirculation zone linearly against the fluctuating energy in the shear layer [40]. Interestingly, the discovery was that an increase in *Re* caused reattachment to shift downstream, a pattern that is in line with the DNS results by Toppings and Yarusevych [41]. The vortex structure is more complex as the Re increases, indicating an increase in Kelvin-Helmholtz instability and a strengthening of the shear layer. There is a small indication of asymmetry at *Re* = 3000, this is biased towards the three-dimensional onset in the flow pattern even though the simulation is conducted in 2D, as warned by Masuda & Tagawa [42] regarding the limitations of prediction at high *Re*.

3.5. Turbulent Kinetic Energy and Eddy Viscosity

Turbulent viscosity field nut which represents the diffusion of momentum due to turbulent fluctuations. At *Re* = 1000, the nut is close to zero in most domains, indicating a dominance of laminar flow or light transitions (Figure 9.a). With the increase in *Re*, especially at *Re* = 2000 and *Re* = 3000, there is a significant increase in the nut value along the shear layer after the step, indicating an increase in turbulence intensity. The peak of the nut at *Re* = 3000 occurs in the shear zone of the developing layer, reflecting the more active production and diffusion of the vortex. According to Choi [43] & Matharu [44], this high eddy viscosity reflects the ability of turbulent models to predict transfer momentum and shear stress in highly separate flows, making nut an important indicator in the validation of a single equation-based RANS model.

The turbulent distribution of kinetic energy *k* (TKE) shown in Figure 9.b shows the maximum production *k* along the post-step shear layer. The increase in Re indicates a larger and wider trend of turbulent energy accumulation. At *Re* = 1000, k production is limited and remains low, corresponding to the absence of large turbulent structures. *Re* = 2000 shows the beginning of the formation of strong fluctuations that develop downstream, while at *Re* = 3000 a high concentration of *k* is seen in the proximal area of the shear layer, indicating the dominance of turbulence production due to high shear stress [45]. Research by Domfeh [5] and Kartashov [46] indicates that accurate *k* prediction is crucial in assessing the performance of turbulent models, especially in geometry with an adverse pressure gradient. Zones with high *k* generally intersect with the region where the velocity gradient is the highest, being a direct indicator of vortex formation and evolution [46].

Turbulent epsilon dissipation rate (TDR) which indicates the region where turbulent energy is converted into internal or internal energy through viscosity. The epsilon pattern is closely correlated with *k,* indicating that the peak of dissipation occurs not far from the area of maximum production of turbulent energy (Figure 9.c). At *Re* = 1000, the epsilon is still low and thinly dispersed, indicating that the flow is still in the early stages of transition. *Re* = 2000 shows a high intensity of dissipation, indicating the presence of a vortex structure that is active in energy diffusion. According to Wang [47] and Rohilla [48], epsilon is a critical parameter in assessing the level of maturity of turbulent flows. The location and intensity of the high epsilon at *Re* = 3000 reinforces the evidence that the turbulent system

is already highly developed with a wide range of energy scales.

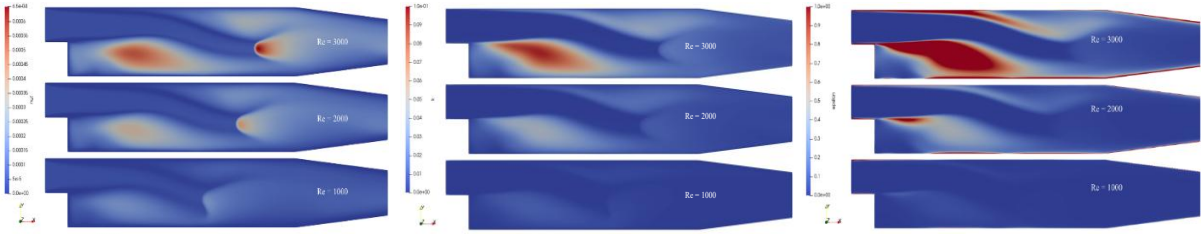

a) b) c)

Figure 9. Profiles of turbulent: (a) viscosity field nut, (b) kinetic energy *k*, and (c) dissipation rate epsilon

4. Conclusion

A comprehensive evaluation of the Reynolds-Averaged Navier-Stokes (RANS) turbulence model for two-dimensional, tune, and uncompressed Backward-Facing Step (BFS) flows in the OpenFOAM framework, with a primary focus on quantifying numerical uncertainty and flow characteristics at Reynolds (*Re*) numbers 1000, 2000, and 3000. Rigorous numerical verification using the Convergence Ratio (*CR*) and Grid Convergence Index (*GCI*) showed that of the three grid configurations tested, only Case 3 (*CR* = 0.54) achieved a valid monotonic convergence, making it the only reliable basis for the uncertainty estimate with a GCI of 0.0059%, while Cases 1 and 2 showed oscillatory and monotonic divergences that were invalid for GCI analysis, respectively. Using the validated grid settings of Case 3, the BFS flow simulation revealed that the normalized longitudinal velocity profile (u/U_{max} vs. y/h) exhibits consistent nondimensional behavior across all *Re*, with a clear backflow region near the step and a rapid recovery towards a fully developed profile at x/h = 6. The incremental increase in the Reynolds number progressively intensified the shear layer gradient, vortex dynamics, and flow remount mechanics, as indicated by the shift of the flow remount point downstream from 0.11 m at *Re* = 1000 to 0.12 m at *Re* = 3000, as well as a significant increase in eddy (nut) viscosity, turbulent kinetic energy (*k*), and the rate of turbulent dissipation (epsilon) along the shear layer. Overall, the study not only provides an advanced assessment of the RANS model but also a rigorous numerical uncertainty analysis, resulting in strong error limits and reproducibility metrics, which decisively contribute to the improvement of CFD predictive accuracy for separate streams and offer practical guidance for engineers and researchers for optimal mesh design, turbulence model selection, and uncertainty management in reliable and geometric BFS simulations related complexes.

Acknowledgments: The authors gratefully acknowledge the invaluable support and facilitation provided by the Head of the Research and Community Service Institute (LPPM) at Universitas Cenderawasih and by the Department of Mechanical Engineering throughout this study.

References

[1] İ. Göktepeli and U. Atmaca, "Numerical Modelling of Backward-Facing Step Flow Via Computational Fluid Dynamics," *Journal of Scientific Reports-A*, no. 054, pp. 176–193, Sep. 2023, doi: 10.59313/jsr-a.1300047.

[2] M. Zhang and X. Song, "Research on the Effects of Nonsmooth Surfaces on Backward-facing Step Flow," *IOP Conf. Ser.: Mater. Sci. Eng.*, vol. 631, no. 2, p. 022019, Oct. 2019, doi: 10.1088/1757-899X/631/2/022019.

[3] S. Mozaffari, M. Visonneau, and J. Wackers, "Average-Based Adaptive Grid Refinement in Hybrid LES," in *Direct and Large Eddy Simulation XII*, vol. 27, M. García-Villalba, H. Kuerten, and M. V. Salvetti, Eds., in ERCOFTAC Series, vol. 27. , Cham: Springer International Publishing, 2020, pp. 449–455. doi: 10.1007/978-3-030-42822-8_59.

[4] A.-K. Ekat, A. Weissenbrunner, M. Straka, T. Eichler, and K. Oberleithner, "Hybrid LES/RANS simulations of a 90° pipe bend using different CFD solvers," *OpenFOAM J*, vol. 3, pp. 49–65, May 2023, doi: 10.51560/ofj.v3.36.
[5] M. K. Domfeh, S. Gyamfi, M. Amo-Boateng, R. Andoh, E. A. Ofosu, and G. Tabor, "Numerical Simulation of an Air-Core Vortex and Its Suppression at an Intake Using OpenFOAM," *Fluids*, vol. 5, no. 4, p. 221, Nov. 2020, doi: 10.3390/fluids5040221.
[6] W. Li, L. Ji, R. Agarwal, W. Shi, and L. Zhou, "Brief Review of Computational Fluid Dynamics," in *Mixed-flow Pumps: Modeling, Simulation, and Measurements*, ASME-Wiley, 2024, pp. 21–46. doi: 10.1115/1.862MFP_ch3.
[7] A. Satheesh Kumar, A. Singh, and K. B. Thiagarajan, "Simulation of backward facing step flow using OpenFOAM®," presented at the Proceedings of the 35th International Conference of the Polymer Processing Society (PPS-35), Cesme-Izmir, Turkey, 2020, p. 030002. doi: 10.1063/1.5141565.
[8] S. Salehi and H. Nilsson, "OpenFOAM for Francis Turbine Transients," *OpenFOAM J*, vol. 1, pp. 47–61, Nov. 2021, doi: 10.51560/ofj.v1.26.
[9] A. Singh, S. Aravind, K. Srinadhi, and B. T. Kannan, "Assessment of Turbulence Models on a Backward Facing Step Flow Using OpenFOAM®," *IOP Conf. Ser.: Mater. Sci. Eng.*, vol. 912, no. 4, p. 042060, Aug. 2020, doi: 10.1088/1757-899X/912/4/042060.
[10] D. Nabapure and R. C. M. K, "DSMC simulation of rarefied gas flow over a 2D backward-facing step in the transitional flow regime: Effect of Mach number and wall temperature," *Proceedings of the Institution of Mechanical Engineers, Part G: Journal of Aerospace Engineering*, vol. 235, no. 7, pp. 825–856, Jun. 2021, doi: 10.1177/0954410020959872.
[11] W.-C. Wu and A. Kumar, "Numerical Investigation of Nanofluid Flow over a Backward Facing Step," *Aerospace*, vol. 9, no. 9, p. 499, Sep. 2022, doi: 10.3390/aerospace9090499.
[12] A. Pont-Vílchez, F. X. Trias, A. Gorobets, and A. Oliva, "Direct numerical simulation of backward-facing step flow at and expansion ratio 2," *J. Fluid Mech.*, vol. 863, pp. 341–363, Mar. 2019, doi: 10.1017/jfm.2018.1000.
[13] A. Bhagat, H. Gijare, and N. Dongari, "Modeling of Knudsen Layer Effects in the Micro-Scale Backward-Facing Step in the Slip Flow Regime," *Micromachines*, vol. 10, no. 2, p. 118, Feb. 2019, doi: 10.3390/mi10020118.
[14] A.-P. Zahiri and E. Roohi, "Assessment of anisotropic minimum-dissipation (AMD) subgrid-scale model: Gently-curved backward-facing step flow," *Int. J. Mod. Phys. C*, vol. 32, no. 05, p. 2150068, May 2021, doi: 10.1142/S0129183121500686.
[15] Y. Sun, H. Qi, G. Zhang, and Y. Wu, "Development and validation of a turbulence model based on drift velocity," *Physics of Fluids*, vol. 36, no. 12, p. 125166, Dec. 2024, doi: 10.1063/5.0245727.
[16] M. Abdollahpour, P. Gualtieri, D. F. Vetsch, and C. Gualtieri, "Numerical Study of Flow Downstream a Step with a Cylinder Part 1: Validation of the Numerical Simulations," *Fluids*, vol. 8, no. 2, p. 55, Feb. 2023, doi: 10.3390/fluids8020055.
[17] T. Mukha, S. Rezaeiravesh, and M. Liefvendahl, "A library for wall-modelled large-eddy simulation based on OpenFOAM technology," *Computer Physics Communications*, vol. 239, pp. 204–224, Jun. 2019, doi: 10.1016/j.cpc.2019.01.016.
[18] A. F. Giyats, M. Yamin, and C. P. Mahandari, "Applied Machine Learning to Estimate Length of Separation and Reattachment Flows as Parameter Active Flow Control in Backward Facing Step," *JMechE*, vol. 20, no. 3, pp. 131–154, Sep. 2023, doi: 10.24191/jmeche.v20i3.23904.
[19] S.-J. Kim *et al.*, "Analysis of the Numerical Grids of a Francis Turbine Model through Grid Convergence Index Method," *kfma*, vol. 23, no. 2, pp. 16–22, Apr. 2020, doi: 10.5293/kfma.2020.23.2.016.
[20] S. Huang, Y. Wei, C. Guo, and W. Kang, "Numerical Simulation and Performance Prediction of Centrifugal Pump's Full Flow Field Based on OpenFOAM," *Processes*, vol. 7, no. 9, p. 605, Sep. 2019, doi: 10.3390/pr7090605.

[21] J. W. Gärtner *et al.*, “Testing Strategies for OpenFOAM Projects,” *OpenFOAM J*, vol. 5, pp. 115–130, Apr. 2025, doi: 10.51560/ofj.v5.134.
[22] F. Jerai, “Accuracy of CFD Simulations on Indoor Air Ventilation: Application of Grid Convergence Index on Underfloor Air Distribution (UFAD) System Design,” *JMechE*, vol. 20, no. 3, pp. 199–222, Sep. 2023, doi: 10.24191/jmeche.v20i3.23908.
[23] T. Bellosta, L. Abergo, and H. Nishikawa, “Enhancing Accuracy in Mixed-Element Grids and Convergence on Skewed Grids for the Two-Dimensional Edge-Based Compressible Navier-Stokes Solver,” in *AIAA SCITECH 2025 Forum*, Orlando, FL: American Institute of Aeronautics and Astronautics, Jan. 2025. doi: 10.2514/6.2025-0072.
[24] S. A. Fallahshams and A. Razani, “Positive solutions to a coupled singular anisotropic system with nonstandard growth and singular nonlinearities,” *Bound Value Probl*, vol. 2025, no. 1, p. 81, Jun. 2025, doi: 10.1186/s13661-025-02072-0.
[25] L. Eça *et al.*, “Assessment of Discretization Uncertainty Estimators Based on Grid Refinement Studies,” *Journal of Verification, Validation and Uncertainty Quantification*, vol. 6, no. 4, p. 041006, Dec. 2021, doi: 10.1115/1.4051477.
[26] F. Zeng, W. Zhang, J. Li, T. Zhang, and C. Yan, “Adaptive Model Refinement Approach for Bayesian Uncertainty Quantification in Turbulence Model,” *AIAA Journal*, vol. 60, no. 6, pp. 3502–3516, Jun. 2022, doi: 10.2514/1.J060889.
[27] H. Xiao and P. Cinnella, “Quantification of model uncertainty in RANS simulations: A review,” *Progress in Aerospace Sciences*, vol. 108, pp. 1–31, Jul. 2019, doi: 10.1016/j.paerosci.2018.10.001.
[28] Y. Ben-Haim and F. Hemez, “Richardson Extrapolation: An Info-Gap Analysis of Numerical Uncertainty,” *Journal of Verification, Validation and Uncertainty Quantification*, vol. 5, no. 2, p. 021004, Jun. 2020, doi: 10.1115/1.4048004.
[29] D. Duong and S. Tavoularis, “Grid-generated velocity fields at very small Reynolds numbers,” *Phys. Rev. Fluids*, vol. 9, no. 2, p. 024607, Feb. 2024, doi: 10.1103/PhysRevFluids.9.024607.
[30] N. Beisiegel, C. E. Castro, and J. Behrens, “Metrics for Performance Quantification of Adaptive Mesh Refinement,” *J Sci Comput*, vol. 87, no. 1, p. 36, Apr. 2021, doi: 10.1007/s10915-021-01423-0.
[31] Z. Liu, F.-B. Tian, and X. Feng, “An efficient geometry-adaptive mesh refinement framework and its application in the immersed boundary lattice Boltzmann method,” *Computer Methods in Applied Mechanics and Engineering*, vol. 392, p. 114662, Mar. 2022, doi: 10.1016/j.cma.2022.114662.
[32] W. L. Oberkampf and C. J. Roy, *Verification, Validation, and Uncertainty Quantification in Scientific Computing*, 2nd ed. Cambridge University Press, 2025. doi: 10.1017/9781009031004.
[33] O. Aycan, A. Topuz, and L. Kadem, “Evaluating uncertainties in CFD simulations of patient-specific aorta models using Grid Convergence Index method,” *Mechanics Research Communications*, vol. 133, p. 104188, Nov. 2023, doi: 10.1016/j.mechrescom.2023.104188.
[34] I. A. Fetuga, O. T. Olakoyejo, D. R. E. Ewim, O. Oluwatusin, A. O. Adelaja, and K. S. Aderemi, “Numerical prediction of flow recirculation length zone in an artery with multiple stenoses at low and high Reynolds number,” *SB*, vol. 36, no. 4, Nov. 2022, doi: 10.7546/SB.03.04.2022.
[35] G. Cui and I. Jacobi, “Prediction of the phase difference between large-scale velocity and Reynolds stress fluctuations in wall turbulence,” *J. Fluid Mech.*, vol. 969, p. A13, Aug. 2023, doi: 10.1017/jfm.2023.565.
[36] H. Abe, Y. Mizobuchi, Y. Matsuo, and P. R. Spalart, “Direct numerical simulation and modeling of a turbulent boundary layer with separation and reattachment,” in *Proceeding of Eighth International Symposium on Turbulence and Shear Flow Phenomena*, Poitiers, Futuroscope, France: Begellhouse, 2013, pp. 1–6. doi: 10.1615/TSFP8.600.
[37] K. Yamamoto, M. Murayama, K. Isotani, Y. Ueno, K. Hayashi, and T. Hirai, “Slat Noise Reduction Based on Turbulence Attenuation Downstream of Shear-layer Reattachment,” in *28th*

AIAA/CEAS Aeroacoustics 2022 Conference, Southampton, UK: American Institute of Aeronautics and Astronautics, Jun. 2022. doi: 10.2514/6.2022-2954.
[38] W. D. Smyth, S. D. Mayor, and Q. Lian, "The Role of Ambient Turbulence in Canopy Wave Generation by Kelvin–Helmholtz Instability," *Boundary-Layer Meteorol*, vol. 187, no. 3, pp. 501–526, Jun. 2023, doi: 10.1007/s10546-022-00765-y.
[39] B. J. Smith, Z. Hussain, S. A. W. Calabretto, and S. J. Garrett, "Laminar boundary layer separation and reattachment on a rotating sphere," *J. Fluid Mech.*, vol. 984, p. A15, Apr. 2024, doi: 10.1017/jfm.2024.173.
[40] Q. Wang *et al.*, "Influence of inner shear layer on the emergence of central recirculation zone in a V-shaped premixed swirling flame," *Physics of Fluids*, vol. 35, no. 10, p. 107129, Oct. 2023, doi: 10.1063/5.0168980.
[41] C. E. Toppings and S. Yarusevych, "Transient dynamics of stall and reattachment at low Reynolds number," *J. Fluid Mech.*, vol. 1011, p. A38, May 2025, doi: 10.1017/jfm.2025.348.
[42] T. Masuda and T. Tagawa, "Effect of Asymmetry of Channels on Flows in Parallel Plates with a Sudden Expansion," *Symmetry*, vol. 13, no. 10, p. 1857, Oct. 2021, doi: 10.3390/sym13101857.
[43] S. W. Choi and H. S. Kim, "Predicting turbulent flows in butterfly valves with the nonlinear eddy viscosity and explicit algebraic Reynolds stress models," *Physics of Fluids*, vol. 32, no. 8, p. 085105, Aug. 2020, doi: 10.1063/5.0006896.
[44] P. Matharu and B. Protas, "Optimal eddy viscosity in closure models for two-dimensional turbulent flows," *Phys. Rev. Fluids*, vol. 7, no. 4, p. 044605, Apr. 2022, doi: 10.1103/PhysRevFluids.7.044605.
[45] Y. Zhang, M. M. Rahman, and G. Chen, "Development of k-R turbulence model for wall-bounded flows," *Aerospace Science and Technology*, vol. 98, p. 105681, Mar. 2020, doi: 10.1016/j.ast.2020.105681.
[46] S. V. Kartashov and Y. V. Kozhukhov, "Substantiation of the various turbulence models use and of the need to account for roughness when calculating the viscous flow in low-flow centrifugal compressor stages using the computational gas dynamics," presented at the International Conference on Science and Applied Science (ICSAS2020), Surakarta, Indonesia, 2020, p. 030054. doi: 10.1063/5.0028248.
[47] Y. Wang, G. Cao, and L. Pan, "Multiple-GPU accelerated high-order gas-kinetic scheme for direct numerical simulation of compressible turbulence," *Journal of Computational Physics*, vol. 476, p. 111899, Mar. 2023, doi: 10.1016/j.jcp.2022.111899.
[48] N. Rohilla, S. Arya, and P. S. Goswami, "Effect of channel dimensions and Reynolds numbers on the turbulence modulation for particle-laden turbulent channel flows," *Physics of Fluids*, vol. 35, no. 5, p. 053323, May 2023, doi: 10.1063/5.0147638.